OPEN ACCESS
Physics of Fluids ARTICLE
The Innovation Energy

Quantifying helium substitution for hydrogen leakage in fuel cell vehicle low-pressure systems: A visual experimental study

Zhonghao Tian,[1] Qingqing Yang,[1,*] Jianwei Li,[1,2] Luqiao Yao,[1] Cong Yin,[3] Hao Tang,[3] and Ricardo Caneloi dos Santos[4]
*Correspondence: qingqing.yang@bath.edu
Received: March 11, 2026; Accepted: July 21, 2026; Published Online: July 23, 2026; https://doi.org/10.59717/j.xinn-energy.2026.100180

GRAPHICAL ABSTRACT

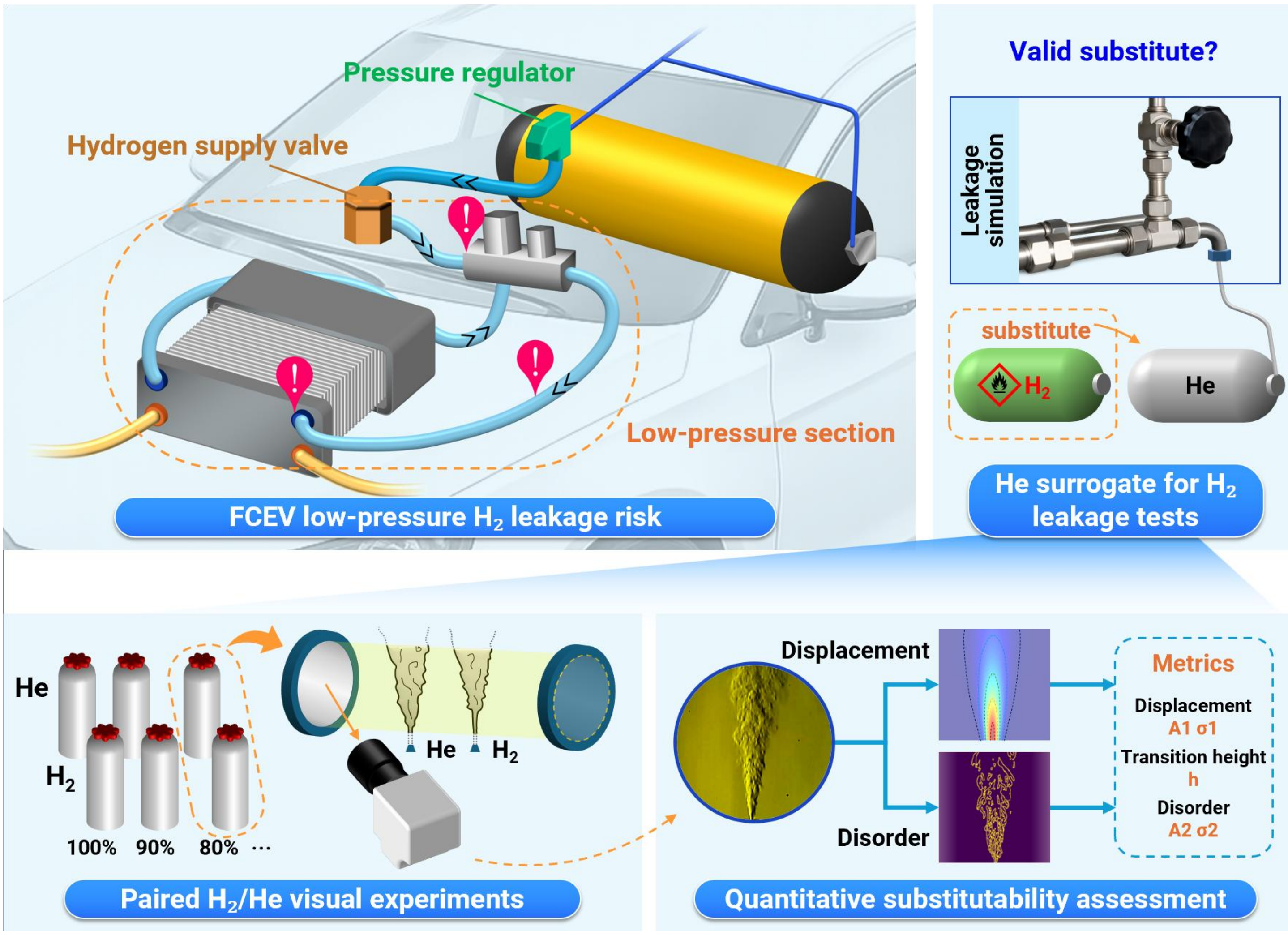

PUBLIC SUMMARY

- Fuel cell vehicle (FCEV) low-pressure hydrogen leaks pose severe safety hazards; helium is widely adopted as surrogate, yet its substitution validity lacks quantitative verification.
- Schlieren tests on vertical hydrogen jets (2–10 SLM, 20–100% concentration) and matching helium cases are carried out to compare leakage diffusion characteristics.
- A displacement-field evaluation method based on schlieren imagery is proposed, and jet transition height follows scaling law linked to Richardson number.
- Equal-buoyancy substitution performs best among three equivalence strategies; a concentration-flowrate formula cuts average relative deviation by 2–3 percentage points.

Quantifying helium substitution for hydrogen leakage in fuel cell vehicle low-pressure systems: A visual experimental study

Zhonghao Tian,[1] Qingqing Yang,[1,*] Jianwei Li,[1,2] Luqiao Yao,[1] Cong Yin,[3] Hao Tang,[3] and Ricardo Caneloi dos Santos[4]

[1]School of Mechanical Engineering, Beijing Institute of Technology, Beijing 100081, China

[2]Beijing Institute of Technology (Zhuhai), Zhuhai 519088, China

[3]University of Electronic Science and Technology of China, Chengdu 611731, China

[4]Federal University of ABC, Santo André CEP 09210-580, Brazil

*Correspondence: qingqing.yang@bath.edu

Received: March 11, 2026; Accepted: July 21, 2026; Published Online: July 23, 2026; https://doi.org/10.59717/j.xinn-energy.2026.100180

Citation: Tian Z., Yang Q., Li J., et al. (2026). Quantifying helium substitution for hydrogen leakage in fuel cell vehicle low-pressure systems: A visual experimental study. *The Innovation Energy* **3**:100180.

Fuel cell vehicle (FCEV) onboard hydrogen system low-pressure leaks are among the main safety risks in real-world operation. Due to hydrogen's flammable and explosive properties, helium is often used as a safe surrogate gas in leakage simulation studies; however, its validity for FCEV-related low-pressure, low-flow leaks has not been quantitatively established. Using a representative vertical free-jet configuration, this study experimentally investigates low-pressure, small-orifice releases relevant to FCEV systems. Schlieren visualization was performed with hydrogen across flowrates of 2–10 standard liters per minute (SLM) and concentrations of 20–100%, and corresponding helium cases were used for substitution analysis. A displacement-field analysis method is proposed to evaluate the substitutability of helium for hydrogen based on the optical information in the schlieren images. The study reveals that the laminar-turbulent transition height of the jet varies with the leakage conditions and is closely correlated with a Richardson-number-based scaling. Three commonly used equivalence strategies are assessed, and the results show that, within the tested conditions, an equal-buoyancy substitution method provides satisfactory accuracy. Furthermore, an empirical substitution formula based on concentration and flowrate is proposed, further reducing the average relative deviation by 2–3 percentage points. This work provides a quantitative framework for the design of helium-based surrogate leakage experiments in hydrogen systems.

INTRODUCTION

Hydrogen is increasingly regarded as a cornerstone of the low-carbon transition.[1-3] According to the International Renewable Energy Agency (IRENA), hydrogen could account for up to 12% of global energy use by 2050.[4] Owing to its high gravimetric energy density and rapid refueling capability,[5] the transport sector is poised to become one of the largest single beneficiaries of low-emission hydrogen.[6,7] The International Energy Agency (IEA) projects that hydrogen and hydrogen-based e-fuels could provide approximately 15% of global transport final energy by 2050 in a Net-Zero Scenario.[8] However, sustained public acceptance and large-scale deployment critically depend on demonstrably safe operation, where unintended hydrogen leakage remains a primary concern[9,10]—particularly hard-to-detect releases in the low-pressure section of FCEV onboard hydrogen systems.[11]

In FCEV onboard hydrogen systems, low-pressure leaks typically occur in pipelines, joints, and valves downstream of the pressure regulator, near the fuel cell stack.[12] These releases can arise from small-orifice defects or sealing issues at fasteners,[13] and are often early-stage, low-flow, and difficult to detect. This poses a significant safety risk because hydrogen has an exceptionally high diffusivity, low ignition temperature (≈ 500 °C), and a wide flammability range (4%–75% by volume in air).[14] Even a small leak can rapidly elevate local hydrogen concentration in confined or semi-confined environments relevant to real operation and servicing (e.g., parking garages, tunnels, and maintenance workshops), potentially reaching the lower explosive limit within seconds and posing a serious threat to both life and property. Despite the need for leakage studies tailored to FCEVs, most existing work has focused on high-pressure releases, while low-pressure, early-stage leaks remain comparatively underexplored.[13,15] At the same time, experiments involving real hydrogen are strongly constrained by technical, financial, and regulatory factors. Full-scale tests are costly, technically complex, and require stringent safety measures,[16] and dedicated jet-release trials demand extensive ventilation, continuous monitoring, and remote handling, imposing substantial logistical burdens.[17] Consequently, surrogate-gas experiments using non-flammable inert gases are often adopted to enable safer and more flexible testing, although their validity for FCEV-relevant low-pressure leakage conditions still requires systematic assessment.

Among various candidate gases, helium is the most widely used surrogate for hydrogen. Numerous researchers have employed helium to simulate hydrogen releases under conditions related to fuel cell applications.[18-20] Although helium is non-flammable and easy to handle, it does not perfectly replicate hydrogen's behavior; discrepancies in buoyancy-driven entrainment and mixing efficiency can lead to differences in flow structure and dispersion range.[21] Therefore, determining how to adjust experimental parameters when substituting helium for hydrogen remains a critical question for improving the accuracy of surrogate testing, especially for FCEV-related low-pressure leakage conditions.

To address this, most substitution studies rely on similarity theories, which aim to match key physical drivers of gas dispersion between helium and hydrogen. Two classical scaling strategies are commonly used: one assumes equal volumetric flowrates, while the other enforces equal buoyancy fluxes to match buoyancy-driving forces. Kokgil[22] developed a theoretical model of point-source light-gas plumes, deriving analytical expressions for plume radius, upward velocity, and density under constant-temperature and proportional entrainment assumptions. A generalized similarity equation for helium-hydrogen plumes was proposed and validated through CFD and sub-scale tests, confirming helium's suitability as a hydrogen surrogate under specific leakage conditions. He et al.[23] used validated CFD models to compare three scaling methods-equal volumetric flow, equal buoyancy, and a novel equal-concentration method-for dispersion in enclosed spaces. Their findings showed that volumetric-flow scaling was effective over longer durations and in areas outside the plume, while buoyancy scaling better captured early convection-driven dynamics. Patel et al.[24] analyzed helium-hydrogen dispersion similarity in semi-confined facilities, showing that without ventilation, equal volumetric flow worked best, whereas at higher ventilation velocities, equal-concentration and equal-buoyancy methods were more accurate. Lacome et al.[25] performed large-scale experiments in an 80 m^3 isothermal confined space, observing rapid ceiling-layer stratification followed by prolonged diffusion to homogeneity, confirming dispersion similarity under isothermal conditions. Chen et al.[26] proposed a polynomial correction algorithm based on hydrogen-helium similarity theory, reducing average concentration error from 14.06% to 7.94% over Reynolds numbers from 3500 to 9500 within 160 s. Despite their widespread use, similarity theories remain imperfect. The equal volumetric flow approach may tend to underperform during early leakage stages, while the equal buoyancy method may lose accuracy over prolonged periods.[23] Limited research has explored the similarity under different initial conditions of early leaks, which are critical to actual leak safety.

Existing hydrogen–helium similarity studies face significant limitations when applied to FCEV leakage. Compared with high-pressure releases, low-pressure leaks downstream of onboard hydrogen systems—typically characterized by near-atmospheric pressure, relatively small volumetric flowrates and partial mixing with ambient air—are more difficult to characterize experimentally, and systematic hydrogen–helium similarity data under such conditions are still scarce. Although CFD models can rapidly produce many simulation data, their predictive accuracy depends on empirical assumptions and calibration and must be verified experimentally. Direct, comprehensive hydrogen–helium leakage experiments under matched conditions are therefore urgently needed, as their absence limits the general applicability of current similarity theories in FCEV scenarios. Additionally, in most similarity experiments, hydrogen concentration fields are sampled using discrete point sensors. While precise, these sensors provide sparse measurements and may disturb the flow, limiting their ability to capture fine-scale dispersion structures. In contrast, schlieren visualization offers a non-intrusive, high-resolution optical technique capable of capturing full-field flow features in real time by imaging refractive-index gradients. It is well suited for observing jet structures and buoyancy-driven dispersion in hydrogen or helium releases, and has been successfully applied in both enclosed and open environments.[27] A previous study developed a calibration method to convert schlieren image gray levels into hydrogen concentration distributions, deriving empirical attenuation relationships in axial and radial directions.[28] Building on that foundation, the present study further exploits schlieren diagnostics as a quantitative tool for assessing hydrogen–helium similarity under FCEV hydrogen system low-pressure leakage conditions.

In this study, we construct a schlieren facility to perform hydrogen and helium leakage tests representative of low-pressure releases in FCEV onboard hydrogen systems. The experimental rig produces near-atmospheric jets with varied initial concentrations and mass flowrates, capturing early-stage, time-resolved schlieren images. We propose a new image-processing workflow that directly fits the displacement field from schlieren image sequences. Based on the extracted displacement fields, we define and compare quantitative flow features, including transition height, for hydrogen and helium cases. These data support the assessment of a quantitative substitution criterion, specifying the helium parameters required to best approximate a given FCEV leakage scenario.

The main contributions of this study are as follows:

1) A novel displacement-field-based quantification method is proposed to extract optical ray displacement fields from schlieren images, enabling quantitative characterization of low-pressure hydrogen leakage characteristics.

2) The transition behavior of the low-pressure jet under varying leakage conditions is identified and characterized, and the two-stage flow features of matched hydrogen and helium leaks are systematically compared.

3) A substitutability assessment framework is developed for hydrogen–helium flow fields, providing guidance for selecting optimal helium experimental parameters in FCEV safety testing.

This paper is organized as follows. Section 2 presents the displacement-field analysis methodology. Section 3 describes the schlieren experimental setup and the details of hydrogen/helium tests. Section 4 introduces the image-processing workflow to extract key jet features. Section 5 reports and discusses the substitutability assessment results. Finally, Section 6 summarizes the main conclusions.

MATERIALS AND METHODS

Methodology of displacement-field analysis

In this section, starting from the Gladstone–Dale relation, we describe a methodology to convert schlieren images of low-pressure hydrogen and helium jets, representative of simplified FCEV leakage, into quantitative displacement fields. This framework provides the theoretical basis for consistently comparing hydrogen and helium leakage jets in the subsequent analysis.

The refractive index n of a gas is linearly related to its density ρ_{gas} through the Gladstone–Dale (G-D) relation:

$$n = 1 + K_{GD}\rho_{gas} \tag{1}$$

where K_{GD} is the Gladstone–Dale constant of the gas. For a gas mixture, the overall refractive index n can be obtained by summing the individual components' K_{GD} values, each weighted by the corresponding partial density within the mixture:[29]

Table 1. Gladstone-Dale constants and gas densities used in this study [29,32]

Gas species	Density	Gladstone–Dale constant
Helium	$0.179\,\mathrm{kgm^{-3}}$	$2.01 \times 10^{-4}\,\mathrm{m^3kg^{-1}}$
Nitrogen	$1.25\,\mathrm{kgm^{-3}}$	$2.38 \times 10^{-4}\,\mathrm{m^3kg^{-1}}$
Air	$1.29\,\mathrm{kgm^{-3}}$	$2.26 \times 10^{-4}\,\mathrm{m^3kg^{-1}}$
Hydrogen	$0.089\,\mathrm{kgm^{-3}}$	$1.47 \times 10^{-4}\,\mathrm{m^3kg^{-1}}$

$$n - 1 = \sum K^i_{GD}\rho^i = \sum K^i_{GD} D^i \phi^i \tag{2}$$

In this expression, the superscript i denotes the i-th gaseous constituent, K^i_{GD} is the Gladstone-Dale constant of the i-th component, ρ^i is its partial density in the mixture, D^i is the density of the corresponding pure component, and φ^i is its mole or volume fraction.

When a gas mixture is released from a round nozzle, it extends upward under the combined influence of buoyancy and initial momentum. In the radial direction, the jet spreads outward from the center. This dispersion process is jointly influenced by molecular diffusion, turbulent mixing, and mean-flow advection, and the diffusion rate is primarily determined by the local concentration gradient $\frac{d\phi_{H_2}}{dr}$.[30] Due to the isotropic structure of the jet in the radial direction, the time-averaged concentration of hydrogen jets at each cross-sectional plane typically follows a Gaussian distribution.[31] In contrast, the instantaneous concentration field exhibits strong spatial and temporal fluctuations due to unsteady turbulent entrainment. The time-averaged concentration distribution at a given axial height z can therefore be approximated as:

$$\phi_{H_2}(x,y) = \phi_{Ce}\exp\left(-\frac{x^2}{2\sigma^2}\right)\exp\left(-\frac{y^2}{2\sigma^2}\right) \tag{3}$$

where σ is the characteristic half-width of the Gaussian distribution, and φ_{Ce} is the centerline volume fraction of released gas. In real-world scenarios involving accidental hydrogen (or non-pure hydrogen) leaks, the resulting jet typically contains only two gaseous components: the released hydrogen and ambient air. However, in laboratory experiments designed to simulate non-pure hydrogen leakage, hydrogen often has to be blended with nitrogen rather than air, in order to ensure experimental safety. As a result, the experimental jet may involve up to three gaseous constituents—hydrogen (or helium), nitrogen, and air. To account for this, the present study models the jet as a ternary gas system in all subsequent theoretical formulations, and the same applies to the two components.

Under the above assumptions, combining Equation (2) and Equation (3) yields the following expression for the local refractive index field. Here, $\eta(0 < \eta \leqslant 1)$ denotes the initial hydrogen volume (or mole) fraction in the source H_2/N_2 mixture, whereas ϕ_{H_2}, ϕ_{N_2}, and ϕ_{air} denote the local volume (or mole) fractions of hydrogen, nitrogen, and ambient air (treated as an independent ambient-gas component) in the jet, respectively:

$$\begin{cases} n = 1 + K_{H_2}D_{H_2}\phi_{H_2} + K_{N_2}D_{N_2}\phi_{N_2} + K_{air}D_{air}\phi_{air} \\ \phi_{H_2}(x,y) = \phi_{Ce}\exp(-\frac{x^2}{2\sigma^2})\exp(-\frac{y^2}{2\sigma^2}) \\ \phi_{N_2} = \frac{\phi_{H_2}}{\eta}(1-\eta) \\ \phi_{air} = 1 - \phi_{H_2} - \phi_{N_2} = 1 - \frac{\phi_{H_2}}{\eta} \end{cases} \tag{4}$$

The Gladstone–Dale constants and gas densities used in this study are summarized in Table 1.

Based on Equation (4), the resulting local refractive index field $n(x,y)$ also follows a two-dimensional Gaussian distribution. It reaches a minimum at the jet centerline and progressively increases toward the ambient-air value with increasing radial distance. This spatial distribution in refractive index arises primarily from the variation in hydrogen concentration, while the contribution of nitrogen to refractive index variation is relatively minor.

When parallel rays are incident, the spatial non-uniformity of the refractive index within the mixed-gas jet causes them to bend. The schlieren system converts this micro displacement into measurable brightness variations in

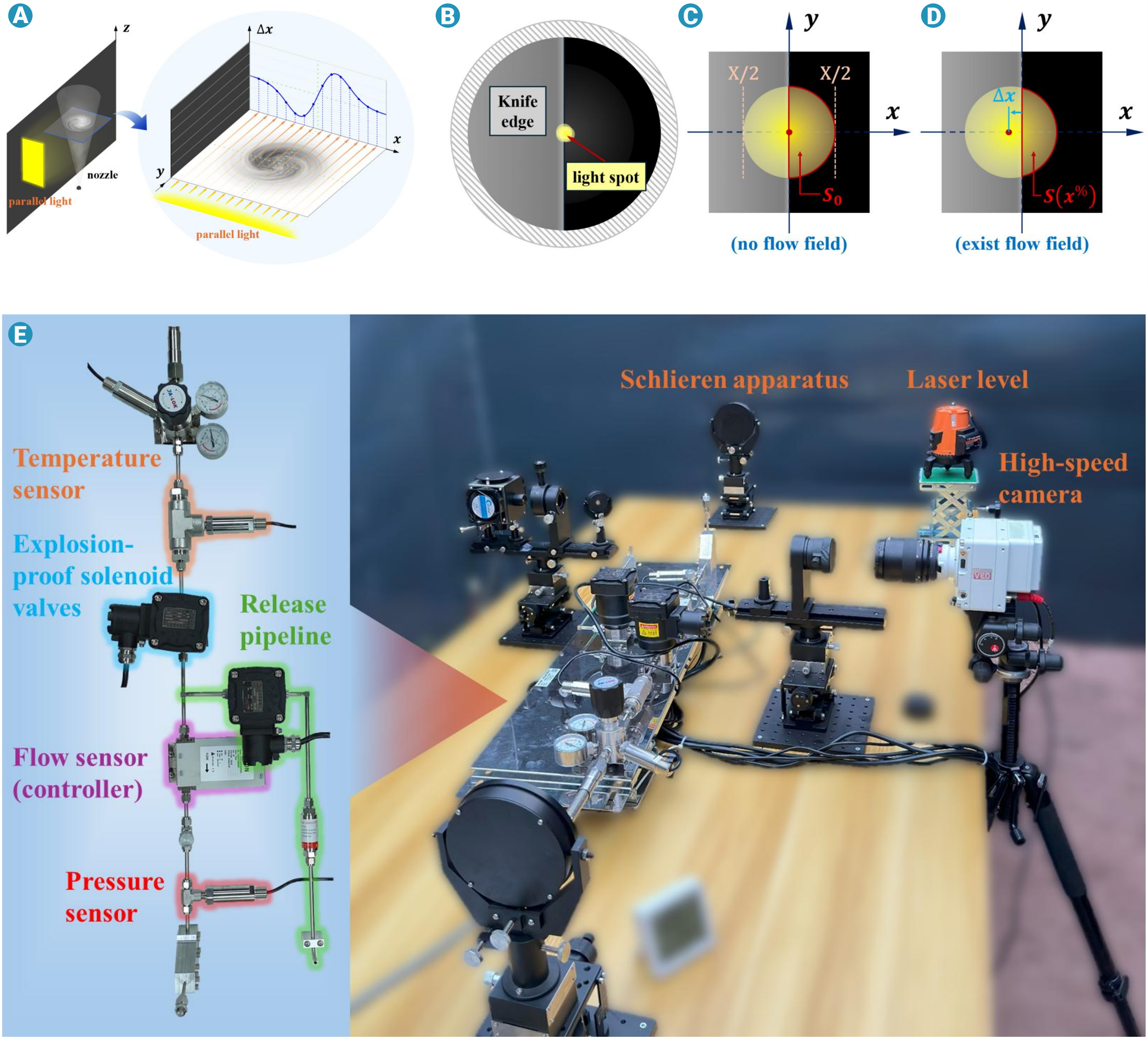

Figure 1. (A) Schematic of schlieren ray deflection induced by refractive index gradients in a light-gas jet. (B-D) Mechanism of brightness formation of schlieren image brightness under ray displacement. (E) Overall experimental setup and gas pipeline configuration.

the recorded image. Figure 1 displays this deflection mechanism using a vertical (z) cross-section. A hydrogen (or helium) jet is ejected upward along the z-axis, while parallel light propagates horizontally in the positive y-direction. In the following, we derive the analytical relationship between the schlieren image brightness and the refractive index distribution. The ray trajectory satisfies the eikonal equation:[33]

$$\frac{d}{ds}\left(n\frac{du}{ds}\right) = \nabla n \tag{5}$$

where s is the arc length along the ray path, and $u(x,y,z)$ denotes the ray displacement vector. From a macroscopic viewpoint, although the light path is slightly deflected within the inhomogeneous flow field, its overall propagation direction remains primarily along the y-axis. Small deflection and displacement only occur in the x- and z-directions. Among these, the deflection in the z-direction is considerably smaller than that in the x-direction. Therefore, the schlieren system is typically configured with a vertically placed knife-edge to record the ray displacement in the x-direction. The eikonal form then simplifies to a quasi-one-dimensional approximation. Applying the small-angle assumption $ds \approx dy$, the governing relation becomes:

$$\frac{d}{dy}\left(n\frac{dx}{dy}\right) = \frac{\partial n}{\partial x} \tag{6}$$

Integrating both sides from $Y_1 = -\infty$ to an arbitrary ordinate y, the lateral displacement is expressed as:

$$n\frac{dx}{dy} = Ax\exp\left(-\frac{x^2}{2\sigma^2}\right)\left[\mathrm{erf}\left(\frac{y}{\sqrt{2}\sigma}\right)+1\right] = \theta(x,y) \tag{7}$$

where $\theta(x,y)$ denotes the integrand introduced for later convenience. The coefficient A encapsulates gas-specific optical and physical parameters, and is given by:

$$A = -\frac{\phi_{Ce}\sqrt{\pi}}{\sqrt{2\sigma^2}\eta}\left(K_{air}\rho_{air} - K_{N_2}\rho_{N_2} + \eta\left[K_{N_2}\rho_{N_2} - K_{H_2}\rho_{H_2}\right]\right) \tag{8}$$

Given the small refractive index variations typical of light-gas jets, the approximation $n \approx 1$ is valid. Under this assumption, the total lateral deflection recorded in the schlieren image simplifies to:

$$\Delta x(x) \approx \int A x \exp\left(-\frac{x^2}{2\sigma^2}\right)\left[\operatorname{erf}\left(\frac{y}{\sqrt{2}\sigma}\right)+1\right] dy = \Theta(x,y) \quad (9)$$

The antiderivative of $\theta(x,y)$ is denoted as $\Theta(x,y)$, which admits a clear physical interpretation: it gives the cumulative lateral displacement, measured at a given ordinate y, of a ray originating at abscissa x and propagates normal to the x-axis. In contrast, $\theta(x,y)$ itself represents the deflection angle of that same ray at the position. For a specified abscissa x_0, the total ray displacement accumulated over the optical path satisfies:

$$\Delta x(x_0) = \Theta(x_0, Y_2) - \Theta(x_0, Y_1) = \int_{Y_1}^{Y_2} \theta(x_0, y)\, dy \quad (10)$$

The lower and upper integration bounds $Y_1 < 0 < Y_2$ correspond to the entry and exit points of a schlieren ray. Since the physical light path is orders of magnitude longer than the width of the helium jet, Y_1 and Y_2 may be taken as $-\infty$ and $+\infty$, respectively.

Moreover, recalling the physical interpretations of $\theta(x,y)$ and $\Theta(x,y)$, a ray that has just entered the flow field possesses neither cumulative displacement nor local deflection. Hence $\theta(x,y)=0$, $\Theta(x,y)=0$. Under these conditions, the total ray displacement is governed predominantly by the plateau region near the upper bound Y_2, where $\theta(Y_2)$ is essentially unchanged. Hence, the integral simplifies to:

$$\Delta x(x_0) = A x_0 exp\left(-\frac{x^2}{2\sigma^2}\right)\int_{Y_1}^{Y_2}[erf\left(\frac{y}{\sqrt{2}\sigma}\right)+1]dy \propto x_0 exp\left(-\frac{x_0^2}{2\sigma^2}\right) \quad (11)$$

In practice, approximating the ray deflection profile by the derivative of a Gaussian is widely adopted.[34] Furthermore, since the schlieren system uses parallel rays, each ray shares identical optical bounds Y_1 and Y_2 (see Figure 1A). In subsequent analysis, deflections are therefore expressed in relative form. Prior to each experiment, the optical system is calibrated such that in quiescent air ($\Delta x = 0$), the knife edge bisects the luminous disc, resulting in half of the incident light being blocked. Assuming a perfectly circular spot, the transmitted luminous flux is then represented by the area as $\frac{S_0}{2}$, where S_0 is the total spot area, as shown in Figure 1B & C. Let X represent the diameter of the light spot. Any ray displacement can then be expressed in non-dimensional form $x^{\%} = \frac{\Delta x}{X}$, and the corresponding relative brightness can be written as:

$$I = \frac{S(x^{\%})}{S_0} = \frac{S(\frac{\Delta x}{X})}{S(0.5)} \quad (12)$$

where $S(x^{\%})$ denotes the luminous area of light passing through, corresponding to the ray displacement $x^{\%}$, as shown in Figure 1D. At this point, a complete forward model from gas concentration—refractive index—ray deflection—schlieren brightness has been established. Conversely, image brightness (greyscale) data can be inverted to recover the ray displacement field. This derived framework forms the theoretical basis for subsequent experimental interpretation and substitutability assessment.

Visualization-based comparative experiments on hydrogen and helium jets

To ensure safety and minimize the influence of environmental disturbances, all experiments designed to emulate key aspects of low-pressure, small-orifice leakage scenarios were conducted inside an open-top safety enclosure. A series of pre-mixed standard hydrogen–nitrogen and helium–nitrogen gases were used, rather than hydrogen–air mixtures, in order to avoid flammability risks. The volume fractions of hydrogen (or helium) in the mixtures were 20%, 30%, 40%, 50%, 60%, 70%, 80%, 90%, and 100%. These mixtures represent hydrogen-rich gases that may arise in low-pressure downstream sections of FCEV hydrogen systems, from partially diluted to pure hydrogen. The experimental layout and pipeline configuration are shown in Figure 2E.

High-pressure gas cylinders were connected to the system, and the downstream pressure was regulated by a pressure-reducing valve installed after the cylinder. After passing through a mass flow controller (MFC), the gas was released into ambient air through a 1 mm-diameter vertical metal nozzle. This nozzle size was selected to represent a typical small-orifice leakage geometry. Similar submillimeter-to-millimeter orifices have been used in hydrogen leakage studies to represent small unintended releases. Under the present low-pressure flow conditions, this diameter produced stable and repeatable jet structures within the schlieren field of view and provided sufficient optical contrast for transition-point identification and post-transition feature extraction.

Hydrogen cases were prescribed over source concentrations of 20–100% and nominal volumetric flowrates of 2–10 SLM, corresponding to the order of magnitude expected for small-orifice leaks in FCEV low-pressure piping.[35] For helium, the operating matrix was extended and offset from the hydrogen matrix to provide sufficient search space for identifying helium cases with corresponding flow-field features in Section 5. Based on preliminary tests and empirical estimates, the helium flowrates were obtained by multiplying the nominal hydrogen flowrate by concentration-dependent factors. The resulting hydrogen and helium flow-rate matrices are summarized in Table S1.

Two explosion-proof solenoid valves independently controlled the opening of the main release path and an emergency bypass pipeline. The main release path mimics a controllable small leak in the low-pressure section of the FCEV onboard hydrogen system, while the bypass pipeline, integrated with a flame arrestor, allows rapid emergency discharge in the event of abnormal operating conditions in the main line, thereby enhancing experimental safety. A high-speed camera was placed on one side of the test platform to record the schlieren visualizations, and temperature and pressure sensors were installed to monitor in-line gas conditions. The entire gas delivery pipeline was designed with explosion-proof protection measures. Key components are labeled in Figure 1E, and their specifications are listed in Table S2.

Experiments were carried out at night to ensure low ambient light and minimal airflow interference. During testing, the ambient temperature was 26.5 °C, relative humidity was 82%, and the illumination intensity at the light source was 16.9 Lx. The distance from the nozzle to the first schlieren mirror was 64 cm. Optical alignment was achieved using a laser level and an optical flat to ensure system horizontality. The nozzle was centered laterally within the schlieren field of view, and the knife edge was mounted vertically. All control components-including the flow controller, solenoid valves, and high-speed camera-were electrically interfaced and operated remotely via a host PC and data acquisition board. During each test run, operators remained at a safe distance of 10 m and remotely initiated the gas injection process at a constant pressure and flowrate. Schlieren images were continuously captured by the high-speed camera at 3000 frames/s, with a total of 1000 frames recorded per trial.

After each run, the remaining gas in the pipeline was purged through the release pipeline. A handheld hydrogen detector was used to confirm complete dissipation of residual hydrogen before replacing gas cylinders and proceeding to the next set of experiments. Throughout the entire testing process, the lighting intensity, nozzle position, and all adjustable components of the schlieren apparatus (e.g., optical alignment, pitch angle) were kept constant to ensure experimental consistency.

RESULTS

Displacement-field analysis of hydrogen and helium jets

In this section, the schlieren data obtained in previous sections are processed into quantitative displacement and disorder fields. This section describes the image-processing workflow and uses the resulting maps to analyze the leakage characteristics of hydrogen and helium jets—particularly jet structure and transition behavior—which provide the basis for the similarity assessment in next section.

The process of generating displacement and disorder maps. Under the same experimental operating procedure, paired hydrogen-helium jet leakage data were obtained for conditions representative of low-pressure leaks in FCEV onboard hydrogen systems. Taking hydrogen as an example, the tests covered 9 initial concentrations and 5 flowrates. One video recording repre-

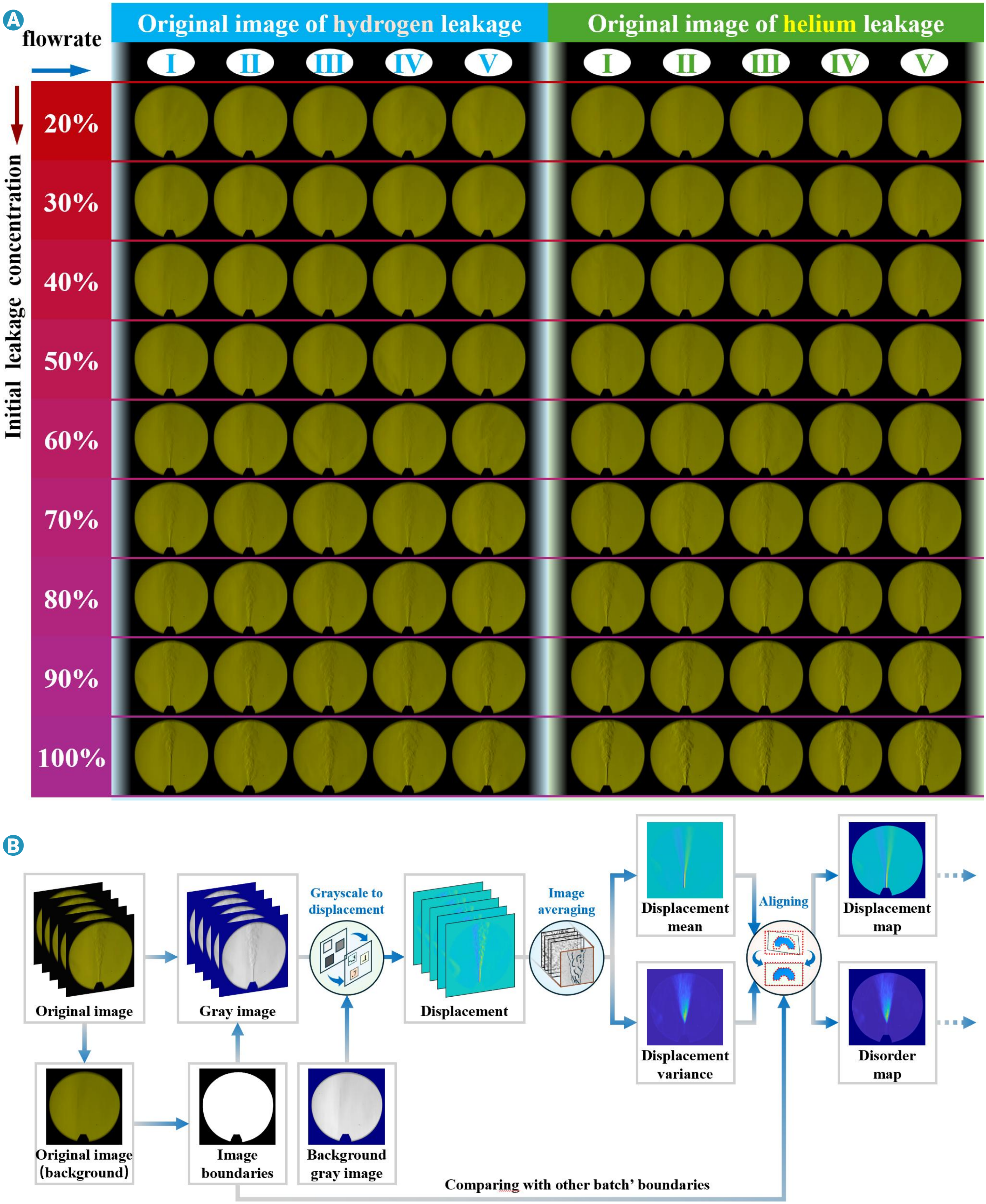

Figure 2. (A) Original schlieren images of hydrogen and helium leaks across varying concentrations (rows) and flowrates (columns). (B) Image processing workflow for extracting displacement and disorder fields from schlieren videos.

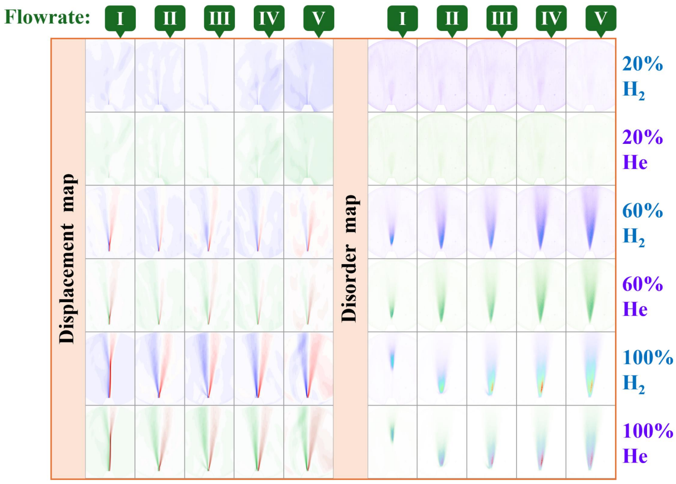

Figure 3. Representative displacement and disorder fields of hydrogen and helium jets.

sents a single-run case, and five runs at the same concentration but different flowrates form a batch. Additionally, a no-jet background case was included in each batch and later used as a reference in image processing. The helium experiments followed the same procedure; therefore, 18 batches were completed in total, yielding 90 single-run schlieren datasets. Each dataset consists of 1000 frames recorded at 330 μs intervals. An overview of raw schlieren images is shown in Figure 2A.

Inspection shows a consistent two-region structure. Near the nozzle the jet is laminar, narrow, and stable; downstream, a laminar-turbulent transition occurs with strong mixing, vortex formation, and jet spreading. At fixed flowrate, higher concentration increases image contrast and spreading angle, while at fixed concentration, higher flowrate enhances fluctuations and shifts the transition upstream.

To extract features, the multi-step image processing shown in Figure 2B was applied: background subtraction, grayscale extraction, schlieren boundary segmentation, displacement reconstruction, disorder quantification, and inter-batch alignment. These yield displacement and disorder maps.

1) Background subtraction and grayscale conversion. The background of each batch was obtained by averaging all frames of its no-jet video. For each single-run dataset, 1000 schlieren frames were converted into grayscale, and a binary segmentation extracted the schlieren boundary.

2) Relative displacement calculation. Each frame was transformed into a displacement field using Equation (12). Background displacement of each batch was subtracted to remove baseline nonuniformities, producing the relative displacement field.

3) Disorder quantification. For each single-run dataset, the mean displacement field was obtained by temporal averaging. Variance across all frames yielded a disorder field representing temporal fluctuations.

4) Cross-batch alignment. To ensure comparability, schlieren boundaries from all batches were aligned to a reference, and the same transformation applied to displacement and disorder datasets.

Displacement-field analysis of hydrogen and helium jets. Following the image processing pipeline outlined in previous section, displacement maps, grayscale maps, and disorder maps were generated for all concentration-flowrate combinations. The average displacement field provides insight into the jet's flow structure and concentration distribution, while the disorder field captures the spatial distribution of turbulent intensity. Representative hydrogen and helium results at 100%, 60%, and 20% initial concentrations are shown in Figure 3.

At high concentrations, lower density weakens initial momentum relative to buoyancy, making the jet sensitive to disturbances. Steep concentration gradients promote diffusion and wide spreading angles; near the transition region, the outer gas layer occasionally detaches, forming a visible "shear peel" pattern. Disorder intensity remains near zero in the laminar region upstream of the transition point but grows downstream, and strong turbulence activity is confined to the jet cone range. Helium shows similar patterns but with clearer schlieren contrast due to a larger refractive index difference with air. At medium concentrations, mixture density approaches air, buoyancy weakens, and momentum dominates. The jet remains stable with smaller spreading angles and lower turbulence. At low concentrations, the mixture density nearly matches that of air, schlieren signals are significantly weakened, and background noise overwhelms the useful features.

Notably, a pronounced "necking" phenomenon is observed in the mean displacement field of the 100% hydrogen case at a flowrate of 4 SLM. Specifically, the jet initially maintains a nearly constant width, then abruptly narrows near the transition point, followed by a rapid radial expansion. This likely results from buoyant stretching, which elongates the jet axially and delays radial diffusion until entrainment disrupts the laminar core, causing the outer high-concentration sheath to detach while the inner jet core remains relatively fast, resulting in a temporary necking near the transition.

It is worth noting that this feature does not exist in cases involving adjacent flowrates or concentrations. At lower flowrates, the greater influence of buoyancy enhances axial stretching and delays the transition further downstream, therefore the transition process tends to proceed in a mild manner. At higher flowrates, the transition point shifts upstream, leaving insufficient space for necking to develop. In such cases, the jet width increases abruptly, due to premature detachment of the outer layer caused by intensified gas-air exchange, leading to increased flow resistance, sudden velocity decay, and localized gas accumulation, which can only disperse radially. At low concentrations, faster mixing and earlier transition also prevent necking. Next section further characterizes transition morphology and quantifies transition height.

Results and discussion of substitutability assessment

To quantitatively establish the correspondence between helium and hydrogen leakage jets under FCEV low-pressure conditions, we extract and compare key jet characteristics on either side of the laminar–turbulent transition. First two sections analyze the dominant features before and after the transition point, respectively; then several helium–hydrogen substitution strategies based on these characteristics are evaluated, and last section discusses the applicability, uncertainty, and implications of helium-based substitution for FCEV safety engineering.

Before the transition point. The most identifiable characteristic is the transition height, defined here as the vertical distance from the nozzle to the location where the coherent laminar jet core breaks down. This transition height serves as a critical feature for comparing hydrogen and helium jets.

The transition point reflects the competition between stability and instability during the laminar–turbulent transformation, representing the combined influence of multiple factors, including initial jet velocity, flowrate, hydrogen concentration, ambient disturbances, and fluid viscosity. In order to quantitatively identify the location of the turning point, the characteristic width parameter σ of the cross-sectional displacement distribution was extracted at each axial position based on the displacement field (the definition of σ appears in Equation (11)). The differential $\Delta\sigma$ between adjacent axial sections was then calculated. For gradual-transition cases, a sustained increase in $\Delta\sigma$ was used to identify the onset of rapid jet broadening. For distinct-transition cases, such as visible necking or abrupt lateral expansion, the transition location was identified from the morphological break and confirmed by the corresponding $\Delta\sigma$ variation, particularly the change of $\Delta\sigma$ from negative or near-zero values to positive values.

Following the identification method described above, the transition heights for all hydrogen and helium datasets were determined. A spatial calibration factor of 0.103 mm per pixel, derived from the schlieren images, was applied to convert these heights from pixels to physical lengths. The resulting values are summarized in Tables S3 & S4. In addition to the tabulated data, the transition heights for both gases under various leakage conditions are visualized as three-dimensional surface plots in Figure 4.

Hydrogen exhibits a sharp transition peak at the lowest tested flowrate (2 SLM) and highest concentration (100%), with a measured transition height of approximately 46.97 mm. At this extreme condition, the extremely low density of hydrogen relative to ambient air and the low flow velocity result in a buoyancy-dominated jet with strong buoyancy tension. Consequently, the laminar core persists longer before breaking down. As the initial concentration decreases from 100% to 20%, the transition height drops dramatically.

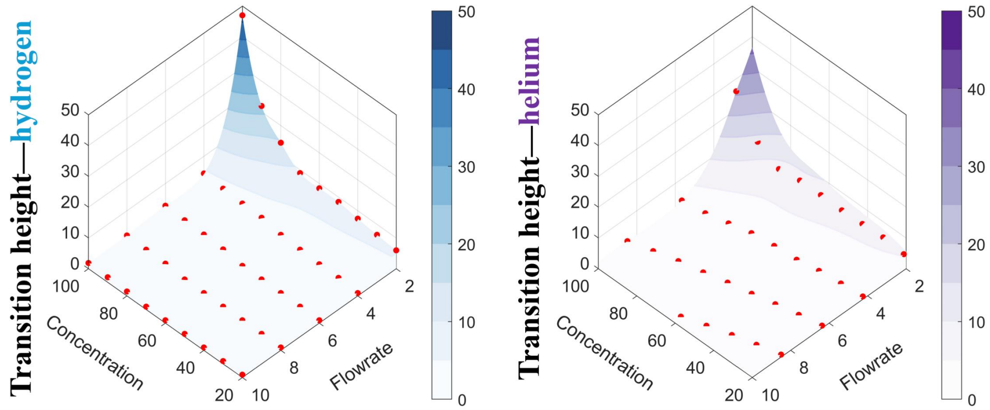

Figure 4. Transition-height surfaces of hydrogen and helium jets under different concentrations and flowrates.

The increasing momentum weakens the influence of buoyancy, and laminar flow stability is more easily disrupted. Similarly, increasing flowrate leads to a drop in transition height, declining along a trajectory close to the exponential trend. When hydrogen concentration falls below 50% or flowrate exceeds 5 SLM, the transition point remains very close to the nozzle and becomes nearly invariant. This clustering reflects the physical behavior of low-concentration jets, for which the transition is governed mainly by momentum-driven mixing rather than buoyancy.

Helium also exhibits the longest laminar section at 100% concentration and the lowest tested flowrate. Moreover, the helium and hydrogen transition-height surfaces show similar overall trends. A possible explanation is that, although the density difference between helium and ambient air is smaller than that between hydrogen and ambient air, helium has a higher dynamic viscosity. Under the present low-pressure, small-orifice leakage conditions, the weaker buoyant acceleration and the stronger viscous effect may partially compensate for each other, causing the transition behaviors of hydrogen and helium to become similar.

As shown in Figure 4, the transition height is jointly affected by the source concentration φ, and the flowrate Q. For the present low-pressure jets, laminar-core breakdown is mainly governed by the competition between injected momentum and buoyancy-induced acceleration. To correlate the measured transition heights, several common single-parameter similarity variables were evaluated. Among them, the Richardson number, $Ri = \frac{g(\rho_a - \rho_0)d}{\rho_0 U_0^2}$ [36] provides an effective measure of this competition by comparing buoyancy and inertia using the nozzle diameter d and the exit velocity U_0 as the characteristic scales. Because the same nozzle geometry was used in all tests, the geometric factors remain constant, making Ri a compact parameter for comparing the relative buoyancy-to-momentum strength of hydrogen and helium jets.

In buoyant jet and plume similarity analyses, characteristic lengths are often described by power-law scalings of the governing dimensionless groups. Accordingly, the transition height was assumed to follow $h \propto Ri^{\alpha}$, where α characterizes the sensitivity of the transition height to buoyancy. The exponent α was fitted from the transition-height surfaces of hydrogen and helium by searching with a resolution of 0.001 and selecting the value that minimized the mean absolute error on the comparison grid (see Figure 4). The resulting best-fit relation is

$$\frac{h_{\mathrm{He}}}{Ri_{He}^{-0.39}(\varphi, Q)} = \frac{h_{H_2}}{Ri_{H_2}^{-0.39}(\varphi, Q)} \tag{13}$$

Equation (13) gave the lowest prediction error among the tested single-parameter correlations, with an MAE of 0.51 mm. This result confirms that the buoyancy-to-momentum ratio is a dominant factor for explaining transition-height variations as the concentration and flowrate change. At the same time, the uncorrected hydrogen-helium transition-height difference is already relatively small, with an MAE of about 0.59 mm, indicating that direct substitution is acceptable for many conditions when only the transition height is considered. The Richardson-number-based correction further reduces the difference and provides a practical way to estimate hydrogen transition heights from helium experiments within the tested range.

After the transition point. For regions above the transition point, the displacement field at each cross-sectional slice is approximately Gaussian derivative in shape. The displacement distribution at any height can be characterized by two parameters: the peak displacement A_1 and the standard deviation σ_1, as defined in Equation (11). Displacement profiles were extracted from cross-sections starting at the nozzle and moving downstream. At each height, the center axis of distribution was identified using a moving window approach, and the sampling region was narrowed to obtain optimal A_1 and σ_1. This process continued until exceeding the image boundary or signal loss. The parameters A_1 and σ_1 characterize the axial and radial decay of jet concentration and are thus used as key features for subsequent analysis.

A similar approach was applied to the disorder fields. Above the transition point, the cross-sectional disorder profile approximately follows a Gaussian shape. At each height, the peak disorder magnitude A_2 and standard deviation σ_2 were extracted through curve fitting. These parameters A_2 and σ_2 represent the evolution of turbulent fluctuation intensity.

Since helium and hydrogen differ in refractive index, their peak displacement magnitudes A_1 and disorder amplitudes A_2 are not directly comparable even under identical concentration distribution conditions. Specifically, helium exhibits stronger schlieren contrast than hydrogen. To enable a fair comparison, normalization was performed on all four parameters A_1, σ_1, A_2, σ_2. A scaling coefficient S was introduced to correct for the refractive index differences. The displacement peak A_1 was divided by S, and the disorder peak A_2 was divided by S^2, thereby aligning the peak intensity baselines of the two gases, called A_1', A_2'. According to Equation (8), the scaling factor S is computed based on the initial gas concentration and σ:

$$S = \frac{1}{\eta}(K_{N_2}\rho_{\mathrm{air}} + K_{\mathrm{air}}\rho_{N_2} - 2K_{\mathrm{air}}\rho_{\mathrm{air}}) + K_{H_2}\rho_{\mathrm{air}} - K_{N_2}\rho_{\mathrm{air}} - K_{\mathrm{air}}\rho_{N_2} + K_{\mathrm{air}}\rho_{H_2} \tag{14}$$

To simplify computation, six cross-sectional slices were sampled at 6 mm intervals, starting from about 10 mm above the transition point and ending at 40 mm. For the concentration maps, the peak value A_1' exhibits a near-linear increase with the initial volume concentration. In contrast, its dependence on flowrate is relatively weak. As height increases, A_1' decreases due to air entrainment and dilution effects. Overall, hydrogen shows slightly higher A_1' values than helium. Notably, the surface at 10 mm above the transition point displays local undulations, which can be attributed to residual influence from the transition morphology, whose shape remains somewhat stochastic at lower altitudes. For instance, distinct depressions are observed in the helium cases of 90-Ⅱ, 90-Ⅰ, 70-Ⅱ, and 60-Ⅰ. This phenomenon occurs due to a sharp transition present in these cases, which tends to appear randomly in leaks with higher concentrations. The abrupt lateral expansion of the jet near the transition point reduces the peak amplitude, leading to the observed depressions. However, as the jet evolves upward, the impact of such localized anomalies gradually diminishes, leading to the flatter distributions observed at 40 mm.

The standard deviation σ_1 in the concentration field exhibits trends complementary to those of A_1'. For example, in regions where the helium A_1' surface shows depressions, σ_1 displays corresponding peaks. And σ_1 reaches local maxima at high concentrations and low flowrates, while remaining relatively flat elsewhere. As the height increases, σ_1 also increases, reflecting the formation of the jet cone structure discussed previously. Overall, hydrogen and helium have comparable σ_1 values near 10 mm, while hydrogen becomes slightly larger at downstream sections. Together with the higher A_1' values of hydrogen, these results indicate that, at the same transition-referenced axial height, the hydrogen jet tends to retain a slightly wider concentration core and a lower cross-sectional mean velocity. This behavior may be attributed to the larger difference between the centerline velocity and the plume-averaged velocity in hydrogen jets, which promotes earlier radial expansion and stronger flow fluctuations.

In contrast to the concentration field, the peak disorder amplitude A_2' exhibits a stronger dependence on the initial concentration. At low axial heights, A_2' decreases rapidly with decreasing initial concentration for both hydrogen and helium, while showing relatively weak sensitivity to flowrate. A prominent ridge forms along the flowrate direction at 100% concentration, indicating the strongest turbulent mixing at high initial concentrations. At this stage, the overall difference between hydrogen and helium remains relatively small, and the two gases exhibit similar surface patterns. As the axial distance from the transition point increases, the high-concentration ridge becomes progressively concentrated toward the high-concentration and high-flow-rate region. At approximately 40 mm above the transition point, both gases still retain relatively high A_2' values near 100% concentration, and their overall trends remain similar. This indicates that the disturbance associated with higher flowrates persists over a longer downstream distance.

For the standard deviation σ_2 of the disorder field, the 10 mm surfaces generally show an increasing trend with gas concentration and a decreasing trend with flowrate, with only small differences between hydrogen and helium. As the height increases, σ_2 becomes larger and more uniform across the surface, whereas the hydrogen surface retains a pronounced local peak under the pure hydrogen, low-flow-rate condition. This indicates that, under this extreme buoyancy-dominated condition, the hydrogen jet undergoes strong lateral expansion and develops broader disorder structures. Such behavior is consistent with enhanced ambient-air entrainment and the overturning or rapid spreading of the jet core in the near field.

Quantitative substitutability assessment based on feature parameters. To evaluate the substitutability of helium for hydrogen, four extracted parameters above the transition point (A_1', σ_1, A_2', and σ_2) are used as indicators. The overall deviation metric is calculated as follows. This calculation method comprehensively accounts for the effects of both the jet's concentration field and random fluctuation field. For most scenarios focusing solely on the concentration field, only the first two terms A_1', σ_1 need be retained.

$$f = \sum_{i=1}^{N} (\Delta A_1' + \Delta\sigma_1 + \Delta A_2' + \Delta\sigma_2)/4N \tag{15}$$

where $\Delta\sigma_1 = \frac{\left|\sigma_1^{H_2} - \sigma_1^{He}\right|}{\sigma_1^{H_2}}$, and similar definitions apply to other terms. For all the hydrogen test cases in the dataset (20–100% in concentration and from 2–10 SLM in flowrate), a constrained nonlinear optimization was performed over the interpolated helium feature surfaces to identify the surrogate condition with the lowest deviation. This process yielded the "optimal surrogate condition" for each hydrogen case. As shown in Figure 6A, due to uncertainties in jet characteristics, the minimum-error helium condition for each hydrogen case still exhibits a random residual error. This residual error includes experimental and other systematic contributions and therefore does not directly represent the intrinsic difference between hydrogen and helium jets; instead, it is more appropriately treated as a baseline, against which the additional errors introduced by specific substitution strategies are evaluated. On this basis, the performance of three commonly used substitution strategies—equal concentration, equal volumetric flowrate, and equal buoyancy flux—is compared against the benchmark. By averaging the relative errors over the entire dataset, the overall performance of each substitution method can be quantitatively assessed, as summarized in Table 2. The common surrogate flowrate is computed using $Q_{He} = Q_{H_2}\left[\frac{\rho_{air} - \rho_{H_2}}{\rho_{air} - \rho_{He}}\right]^n$ (n=0, 1/2, 1).[22]

The results indicate that, despite stochastic variability associated with transition randomness, all three classical methods provide reasonably close estimates for the FCEV low-pressure leaks considered in this study. The equal-flowrate, equal-concentration, and equal-buoyancy methods produce relative deviations of 0.148, 0.143, and 0.140, respectively, corresponding to excess deviations of 0.063, 0.059, and 0.056 above the benchmark. When disorder-related parameters are excluded and only concentration-field features are considered, the corresponding deviations decrease to 0.125, 0.123, and 0.122. Among these strategies, the equal-buoyancy method yields the lowest overall deviation for the present vertical low-pressure light-gas jets, as illustrated in Figure 6B. However, its applicability becomes limited under strongly buoyancy-dominated conditions, as discussed later.

For low-Reynolds-number, low-pressure hydrogen and helium jets in the early stage, this comparison suggests a natural refinement of the empirical substitution rule. Since the three classical methods can all be expressed as power-law corrections based on the density-difference ratio, the present work retains this physically interpretable form. To better account for the coupled effects of source concentration and buoyancy-momentum competition, the empirical relation is extended to include two fitted exponents, n^Q and n^ϕ, for the helium flowrate and source concentration, respectively.

$$\begin{cases} Q_{He} = Q_{H_2}\left[\frac{\rho_{air} - \rho_{H_2}}{\rho_{air} - \rho_{He}}\right]^{1.4} \\ \phi_{He} = \phi_{H_2}\left[\frac{\rho_{air} - \rho_{H_2}}{\rho_{air} - \rho_{He}}\right]^{0.7} \end{cases} \tag{16}$$

The exponents in Equation (16) were obtained by searching for the combination of n^Q and n^ϕ that gave the smallest overall feature deviation across all hydrogen operating conditions. Specifically, n^Q and n^ϕ were searched with a step size of 0.1, and the helium concentration was constrained not to exceed the physical upper limit of 100%. The resulting values were $n^Q = 1.4$ and $n^\phi = 0.7$.

As shown in Figure 6C, the empirical correction further reduces the deviation relative to the classical substitution rules. The average relative deviation decreases to 0.117 (with an excess deviation of 0.032 above the benchmark). When only concentration-field parameters are considered, the deviation is further reduced to 0.093, which is also lower than those of the three classical strategies. Therefore, Equation (16) provides a practical rule for selecting helium test conditions for the present FCEV low-pressure leakage configuration.

Discussion of applicability of helium-based substitution. The present results indicate that helium can serve as a surrogate for hydrogen under the low-pressure, near-field free-jet conditions considered in this study. The hydrogen leakage experiments were conducted for vertical jets released from a 1 mm round orifice, with flowrates of 2–10 SLM and initial volume fractions of 20–100%, in an unobstructed quiescent environment. Within this range, the transition-point heights of hydrogen and helium were generally close, with a MAE of 0.59 mm, indicating similar near-field transition behavior in most tested cases. When the Richardson-number-based correction in Equarion (13) is applied to the transition height, the deviation can be further reduced.

Above the transition point, the feature-based comparison further shows that the three common substitution strategies provide acceptable approximations when high accuracy is not required. Among them, the equal-buoyancy method shows a slight advantage in reproducing the post-transition plume characteristics. These results suggest that helium-based substitution can provide useful first-order guidance for FCEV low-pressure leakage simulations, particularly when the objective is to reproduce the overall plume structure rather than exact local concentration fields.

To assess the robustness of these results, an uncertainty and sensitivity analysis was conducted for the transition height, fitted post-transition features, and final substitution metrics. The main uncertainty sources considered were image calibration, transition-position resolution, mass-flow-controller accuracy, gas concentration tolerance, and curve-fitting uncertainty. The largest relative uncertainty in transition height occurs for near-nozzle transition cases, where the relative uncertainty is about 5.7–6.4%. For

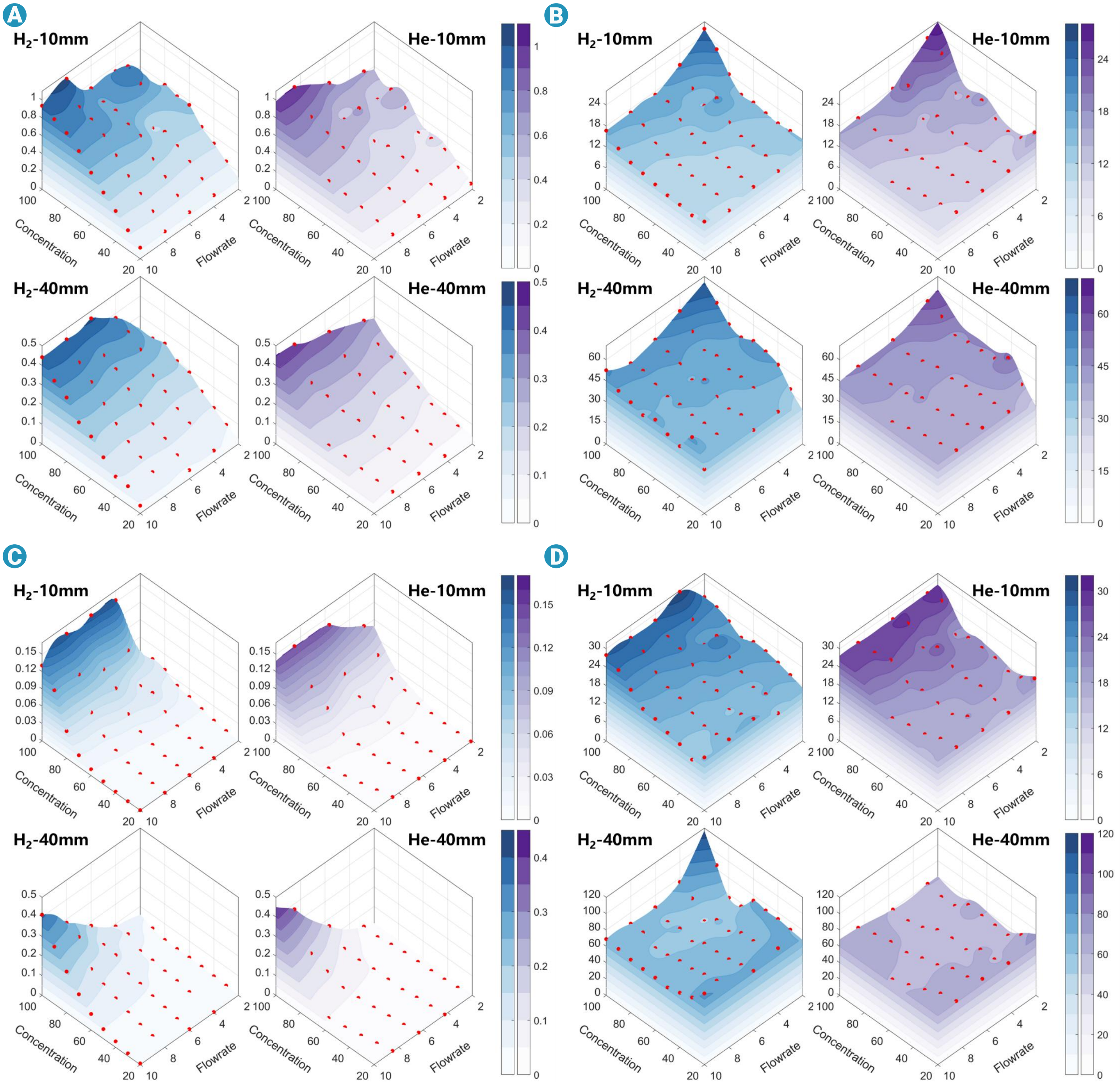

Figure 5. (A) Concentration peak values A_1' for hydrogen and helium. (B) Concentration standard deviation σ_1 for hydrogen and helium. (C) Disorder peak values A_2' for hydrogen and helium. (D) Disorder standard deviation σ_2 for hydrogen and helium.

larger transition heights, the relative uncertainty decreases substantially. In addition, Monte Carlo perturbation of the specified flowrate and concentration uncertainties yielded empirical-formula mean full and concentration-only deviations of 0.1332 ± 0.0056 and 0.1033 ± 0.0045, respectively, compared with the unperturbed baseline values of 0.1168 and 0.0931. Although the Monte Carlo means are slightly higher than the baseline values, the uncertainty intervals remain relatively narrow. Therefore, the propagated uncertainties do not change the relative ranking of the helium substitution strategies and do not affect the main conclusions of the present study. It should also be noted that the present conclusions are directly applicable to $H_2(N_2)$ and $He(N_2)$ premixed leakage cases. If the results are directly extended to H_2(air) premixed cases, the diluent-related optical difference may lead to an equivalent initial-concentration offset of at most 2%. This offset can be eliminated by adjusting the actual $H_2(N_2)$ concentration to an equivalent H_2(air) concentration that produces the same refractive index.

However, for extreme buoyancy-dominated conditions, helium may no longer provide a reliable surrogate for hydrogen leakage. In the present experimental matrix, the 100% H_2 case at 2 SLM corresponds to the largest Richardson number, $Ri \approx 7.35 \times 10^{-5}$, and also produces the largest deviation in the helium-search procedure. Other cases with Ri approaching 3×10^{-5}, such as 90% H_2 at 2 SLM, also exhibit increased substitution errors. Therefore, within the present experimental configuration, helium substitution should be used with caution when Ri approaches 3×10^{-5} and should not be considered reliable when Ri exceeds approximately 5×10^{-5}. Under such strongly buoyancy-dominated conditions, the buoyancy-driven jet dynamics of hydrogen and helium differ sufficiently that no practically acceptable

Table 2. Average relative deviations obtained by different substitution methods

	Relative Deviation	Excess over benchmark	Relative Deviation (concentration only)	Excess over benchmark
Optimal Surrogate (benchmark)	0.084	-	0.048	-
Equal Flowrate (n=0)	0.148	0.063	0.125	0.077
Equal Concentration (n=1/2)	0.143	0.059	0.123	0.076
Equal Buoyancy (n=1)	0.140	0.056	0.122	0.074
Empirical Formula (present work)	0.117	0.032	0.093	0.045

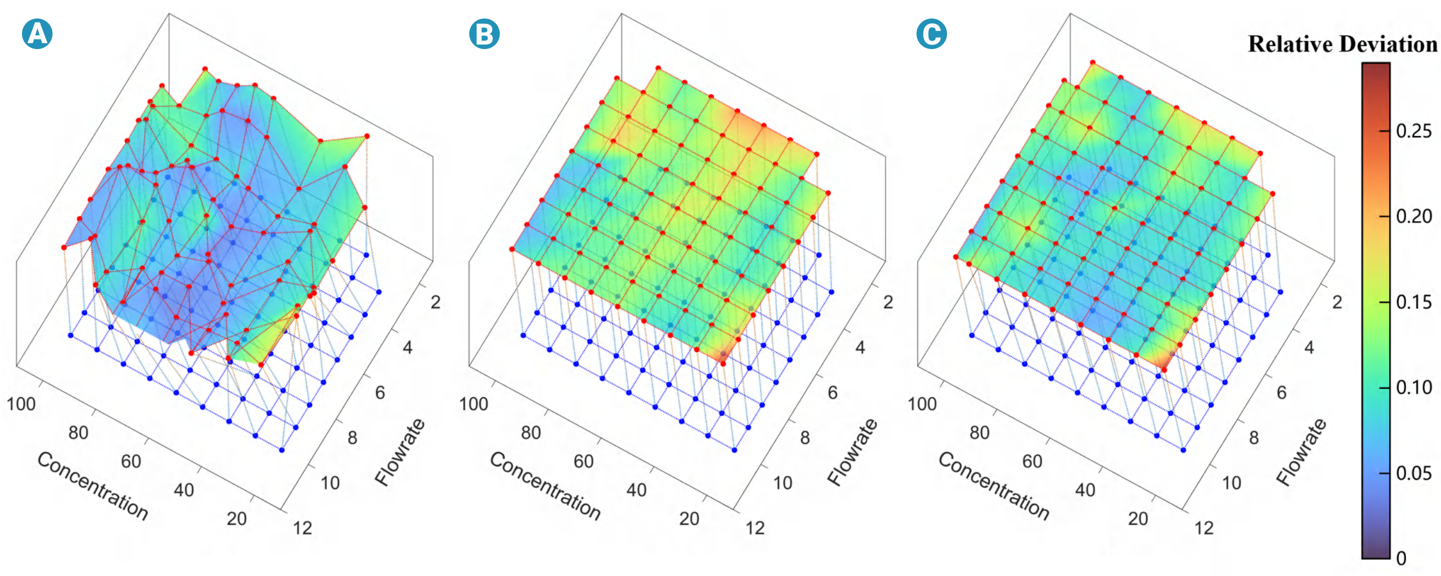

Figure 6. Relative deviation results of hydrogen-helium substitution under different methods.

helium surrogate condition can be identified within the tested helium dataset.

In addition, its applicability to practical FCEV layouts depends on whether the surrounding geometry alters the near-field jet. The present relation is most directly applicable when nearby walls, components, or ventilation flows do not intersect or substantially deflect the first few centimeters downstream of the release. Under weak confinement or moderate ventilation, it may still serve as a baseline, although additional corrections for obstacle proximity or crossflow effects may be needed.[37,38] By contrast, strongly confined spaces, direct impingement, wall-attached releases, or strong ventilation require geometry-specific experiments or CFD validation rather than direct use of the free-jet substitution relation.

The proposed empirical formula was calibrated only for the 1 mm orifice condition. Changes in orifice diameter can alter the exit velocity and thus modify the momentum-buoyancy balance, which may shift the transition location and subsequent plume development. Accordingly, for other leakage diameters, Equation (13) and Equation (16) should be treated only as a first-order estimate unless dynamic similarity is maintained. A more rigorous extrapolation would require a scaling approach in which the key governing dimensionless parameters, particularly the Reynolds number and Richardson number, are matched between the reference and target conditions.[35,39]

Despite these limitations, the findings have practical implications for hydrogen safety assessment. The quantified transition height provides a reference for identifying where significant diffusion and turbulent mixing begin, which may inform sensor placement in low-pressure leakage scenarios. In addition, the full field schlieren measurements and reconstructed displacement fields provide benchmark data for CFD validation under comparable boundary conditions. Overall, the present results support helium-based testing within a defined range of FCEV-relevant low-pressure leakage conditions, while clarifying the regimes in which direct substitution may become unreliable.

CONCLUSION

In this study, a visual displacement-field analysis method is developed to systematically evaluate the substitutability of helium for hydrogen in simulating low-pressure leaks in FCEV onboard hydrogen systems. Based on hydrogen leakage schlieren experiments under a representative set of FCEV low-pressure, low-flow small-orifice leakage conditions (flowrates of 2–10 SLM and initial hydrogen concentrations of 20–100%) and paired helium experiments, two-stage flow features of matched hydrogen and helium jets are systematically analyzed and compared. The results show that, under moderate accuracy requirements, near-field helium jets can approximately substitute for hydrogen jets in both the laminar-transition region and the post-transition plume region. Relating the laminar-turbulent transition height to the Richardson number raised to the power of -0.39 enables effective prediction of hydrogen jet development. By comparing three common substitution strategies—equal concentration, equal volumetric flowrate, and equal buoyancy flux—it is shown that, for FCEV leakage tests with moderate accuracy requirements, a buoyancy flux criterion provides a convenient replacement; however, under strongly buoyancy-dominated conditions, namely high hydrogen concentration and very low flowrate, the behavior of hydrogen jets remains difficult to replicate with helium, and helium-based substitution should be applied with caution. Building on these results, an empirical surrogate formula proposed in this work, combining concentration and flowrate, further improves the matching accuracy. Furthermore, this work provides key experimental data and theoretical tools for hydrogen leakage testing standardization in FCEVs, thereby facilitating safer design and operation.

REFERENCES

1. Zhou B. (2024). Liquid hydrogen carriers: Linking renewable energies for a carbon-neutral future. *Innov. Energy* **1**:100020. DOI:10.59717/j.xinn-energy.2024.100020
2. Lyu S., Huang X., Peng S., et al. (2024). A novel method for analyzing the leakage and diffusion of hydrogen: first arrival time distribution. *Renew. Sustain. Energy Rev.* **198**:114451. DOI:10.1016/j.rser.2024.114451

3. Ocko I.B. and Hamburg S.P. (2022). Climate consequences of hydrogen emissions. *Atmos. Chem. Phys.* 22:9349–9368. DOI:10.5194/acp-22-9349-2022
4. IRENA. (2022). Hydrogen 2022. Available from: https://www.irena.org/Energy-Transition/Technology/Hydrogen
5. Zhang L., Jia C., Bai F., et al. (2024). A comprehensive review of the promising clean energy carrier: hydrogen production, transportation, storage, and utilization (HPTSU) technologies. *Fuel* 355:129455. DOI:10.1016/j.fuel.2023.129455
6. Yao N., Ma T., Lin W., et al. (2025). In-situ estimation of nitrogen concentration in fuel cell systems via anode pressure drop modeling. *eTransportation* 25:100444. DOI:10.1016/j.etran.2025.100444
7. Wallington T.J., Woody M., Lewis G.M., et al. (2024). Green hydrogen pathways, energy efficiencies, and intensities for ground, air, and marine transportation. *Joule* 8:2190–2207. DOI:10.1016/j.joule.2024.07.012
8. IEA. (2023). Net zero roadmap: a global pathway to keep the 1.5 °C goal in reach – analysis. Available from: https://www.iea.org/reports/net-zero-roadmap-a-global-pathway-to-keep-the-15-c-goal-in-reach
9. Li J., Liu J., Dai H., et al. (2024). Rapid development of hydrogen in the energy sector raises safety regulatory concerns. *Innov. Energy* 1:100037. DOI:10.59717/j.xinn-energy.2024.100037
10. Greene D.L., Ogden J.M. and Lin Z. (2020). Challenges in the designing, planning and deployment of hydrogen refueling infrastructure for fuel cell electric vehicles. *eTransportation* 6:100086. DOI:10.1016/j.etran.2020.100086
11. Yang L., Li J., Liang H., et al. (2026). Risk quantification assessment for fuel cell buses based on component leakage space risk analysis. *Renew. Energy* 256:124046. DOI:10.1016/j.renene.2025.124046
12. Wang T., Yang F., Hu Q., et al. (2022). Experimental and simulation research on hydrogen leakage of double ferrule joints. *Process Saf. Environ. Prot.* 160:839–846. DOI:10.1016/j.psep.2022.02.056
13. Gitushi K.M., Blaylock M.L. and Klebanoff L.E. (2022). Hydrogen gas dispersion studies for hydrogen fuel cell vessels II: fuel cell room releases and the influence of ventilation. *Int. J. Hydrogen Energy* 47:21492–21505. DOI:10.1016/j.ijhydene.2022.04.263
14. Li Y., Wang Z., Shi X., et al. (2023). Safety analysis of hydrogen leakage accident with a mobile hydrogen refueling station. *Process Saf. Environ. Prot.* 171:619–629. DOI:10.1016/j.psep.2023.01.051
15. Liu S. and He R. (2024). Decision-level fusion detection method of hydrogen leakage in hydrogen supply system of fuel cell truck. *Fuel* 367:131455. DOI:10.1016/j.fuel.2024.131455
16. Groethe M., Merilo E., Colton J., et al. (2007). Large-scale hydrogen deflagrations and detonations. *Int. J. Hydrogen Energy* 32:2125–2133. DOI:10.1016/j.ijhydene.2007.04.016
17. Daubech J., Hebrard J., Jallais S., et al. (2015). Un-ignited and ignited high pressure hydrogen releases: concentration – turbulence mapping and overpressure effects. *J. Loss Prev. Process Ind.* 36:439–446. DOI:10.1016/j.jlp.2015.05.013
18. Liu H., Salehi F. and Abbassi R. (2023). Experimental and numerical analysis of low-density gas dispersion characteristics in semi-confined environments. *J. Loss Prev. Process Ind.* 86:105184. DOI:10.1016/j.jlp.2023.105184
19. Xin J., Duan Q., Jin K., et al. (2023). A reduced-scale experimental study of dispersion characteristics of hydrogen leakage in an underground parking garage. *Int. J. Hydrogen Energy* 48:16936–16948. DOI:10.1016/j.ijhydene.2023.01.170
20. Kim B. and Hwang K.-I. (2024). Influence of air changes per hour on hydrogen leaks in mechanically ventilated enclosures. *J. Build. Eng.* 88:109071. DOI:10.1016/j.jobe.2024.109071
21. Oamjee A. and Sadanandan R. (2022). Suitability of helium gas as surrogate fuel for hydrogen in H2-air non-reactive supersonic mixing studies. *Int. J. Hydrogen Energy* 47:9408–9421. DOI:10.1016/j.ijhydene.2022.01.022
22. Kokgil E. (2015). Using helium as hydrogen surrogate for safety analysis related to hydrogen leaks from residential fuel cell [Master thesis]. Concordia University.
23. He J., Kokgil E., Wang L. (Leon), et al. (2016). Assessment of similarity relations using helium for prediction of hydrogen dispersion and safety in an enclosure. *Int. J. Hydrogen Energy* 41:15388–15398. DOI:10.1016/j.ijhydene.2016.07.033
24. Patel P., Garaniya V., Baalisampang T., et al. (2024). A computational analysis of similarity relations using helium as a surrogate of hydrogen in semi-confined facilities. *Int. J. Hydrogen Energy* 91:1113–1126. DOI:10.1016/j.ijhydene.2024.10.071
25. Lacome J.M., Jamois D., Perrette L., et al. (2011). Large-scale hydrogen release in an isothermal confined area. *Int. J. Hydrogen Energy* 36:2302–2312. DOI:10.1016/j.ijhydene.2010.10.080
26. Chen L., Hong Y., Qi W., et al. (2024). The method to improve the accuracy of experiment using helium instead of hydrogen. *Int. J. Hydrogen Energy* 78:244–255. DOI:10.1016/j.ijhydene.2024.06.223
27. Chu W.-L., Zhou J.-M. and Jian B.-L. (2025). Leveraging dynamic color schlieren imaging for enhanced airflow velocity prediction. *IEEE Sensors J.* 25:2341–2351. DOI:10.1109/JSEN.2024.3504564
28. Li J., Tian Z., Yang Q., et al. (2023). A new visual approach with the concentration calibration method for the hydrogen leakage and distribution research. *Fuel* 346:128132. DOI:10.1016/j.fuel.2023.128132
29. Ghazwani H. (2016). Preliminary Study of Optical-Flow Based Background-Oriented Schlieren Measurements [Master thesis]. Western Michigan University.
30. Lim H.D. and Vanderwel C. (2025). Application of turbulent diffusivity models to point-source dispersion in outdoor and indoor flows. *Int. J. Heat Fluid Flow* 115:109833. DOI:10.1016/j.ijheatfluidflow.2025.109833
31. Veser A., Kuznetsov M., Fast G., et al. (2011). The structure and flame propagation regimes in turbulent hydrogen jets. *Int. J. Hydrogen Energy* 36:2351–2359. DOI:10.1016/j.ijhydene.2010.03.123
32. Schmidt B.E., Bathel B.F., Grauer S.J., et al. (2025). Twenty-five years of background-oriented schlieren: advances and novel applications. *AIAA SCITECH*. DOI:10.2514/6.2025-1627
33. Grauer S.J., Unterberger A., Rittler A., et al. (2018). Instantaneous 3D flame imaging by background-oriented schlieren tomography. *Combust. Flame* 196:284–299. DOI:10.1016/j.combustflame.2018.06.022
34. Yang F., Wang T., Deng X., et al. (2021). Review on hydrogen safety issues: Incident statistics, hydrogen diffusion, and detonation process. *Int. J. Hydrogen Energy* 46:31467–31488. DOI:10.1016/j.ijhydene.2021.07.005
35. Houf W. and Schefer R. (2008). Analytical and experimental investigation of small-scale unintended releases of hydrogen. *Int. J. Hydrogen Energy* 33:1435–1444. DOI:10.1016/j.ijhydene.2007.11.031
36. He S., Xu Z. and Jackson J.D. (2002). An experimental investigation of buoyancy-opposed wall jet flow. *Int. J. Heat Fluid Flow* 23:487–496. DOI:10.1016/S0142-727X(01)00152-7
37. Hou X., Lan H., Zhao Z., et al. (2023). Effect of obstacle location on hydrogen dispersion in a hydrogen fuel cell bus with natural and mechanical ventilation. *Process Saf. Environ. Prot.* 171:995–1008. DOI:10.1016/j.psep.2022.12.094
38. Li Y., Hou X., Wang C., et al. (2022). Modeling and analysis of hydrogen diffusion in an enclosed fuel cell vehicle with obstacles. *Int. J. Hydrogen Energy* 47:5745–5756. DOI:10.1016/j.ijhydene.2021.11.205
39. Soleimani nia M., Maxwell B., Oshkai P., et al. (2018). Experimental and numerical investigation of turbulent jets issuing through a realistic pipeline geometry: Asymmetry effects for air, helium, and hydrogen. *Int. J. Hydrogen Energy* 43:9379–9398. DOI:10.1016/j.ijhydene.2018.03.197

AUTHOR CONTRIBUTIONS

All authors contributed to the manuscript and approved the final version.

DECLARATION OF INTERESTS

The authors declare no competing interests.

DATA AND CODE AVAILABILITY

Data are available from the corresponding author upon reasonable request.

SUPPLEMENTAL INFORMATION

It can be found online at: https://doi.org/10.59717/j.xinn-energy.2026.100180